

Radiomics analysis to predict pulmonary nodule malignancy using machine learning approaches

Warkentin MT, Al-Sawaihey H, Lam S, Liu G,
Diergaarde B, Yuan J, Wilson DO, Tammemägi MC,
Atkar-Khattra S, Grant B, Brhane Y, Khodayari-Moez E,
Tammemägi MC, Campbell KR, Hung RJ

Supplementary Methods

1	Computed tomography baseline screening protocol	2
1.1	National Lung Screening Trial	2
1.2	PanCanadian Early Detection of Lung Cancer Study	2
1.3	International Early Lung Cancer Action Program - Toronto	2
1.4	Pittsburgh Lung Screening Study	2
2	Semi-automated pulmonary nodule segmentation	3
3	Ground-truth nodule malignancy status	5
4	Initial filtering of radiomics features	6
5	Application of the PanCan Model	7
	References	8

1 Computed tomography baseline screening protocol

The following sections will briefly describe the CT screening protocol used in each of the four lung cancer screening studies.

1.1 National Lung Screening Trial

CT screening was done using multi-detector scanners (at least four detectors) for a helical acquisition with the participant in the supine position (arms elevated above the head) with suspended maximal inspiration with the following acquisition settings: 120 to 140 kVp voltage, 40 to 80 mA current, 2.5mm detector collimation, 1.0 to 3.2 mm nominal reconstructed section width, 1.0 to 2.5 reconstruction interval, 25 second scanning time, and a soft tissue or thin section reconstruction kernel. All low-dose CT scanners were certified for use in the NLST by meeting the acquisition requirements described previously. More details can be found in¹.

1.2 PanCanadian Early Detection of Lung Cancer Study

Screening was performed during a single inspiratory breath hold with the participant in a supine position. PanCan used multi-detector row CT scanners (minimum of four detectors) with a reconstruction interval (i.e., slice thickness) in the trans-axial plane of 1.25mm or less, and within-plane spacing of 1.25mm or less. PanCan used different reconstruction algorithms (kernels), one for lung parenchyma, and another for visualizing mediastinal structures. Scans were performed with 120kV, 40 to 50 mAs, and a rotation time of less than 1 second. Each scan was reviewed by a designated radiologist for each participating centre. More details can be found in² and³.

1.3 International Early Lung Cancer Action Program - Toronto

Baseline CT scans for IELCAP-Toronto were acquired using multi-detector-row CT scanners with 16 or more rows and 4 to 64 channels. Low-dose, thin-slice CT scans were performed using the following acquisition settings: axial reconstruction slice thickness at 1.25mm or less, 120 kVp or lower, 40 to 60 mAs, and a non-edge enhancing image reconstruction kernel. Radiologists reviewed scans at the Toronto site, aware of which screening round (baseline or repeat) the scan belongs to. The primary objective for the baseline scans was to identify all non-calcified nodules. More details can be found in⁴.

1.4 Pittsburgh Lung Screening Study

Screening was performed using a single-breath-hold, helical, low-dose technique (40-60 mA, 140 kVp) to obtain axial reconstructions with slice thickness of 2.5mm intervals. PLuSS used a high-spatial frequency lung kernel at contiguous 2.5mm intervals. All scans were reviewed by one of two study radiologists using standard lung windows. More details can be found in⁵.

2 Semi-automated pulmonary nodule segmentation

We performed supervised semi-automated segmentations of screen-detected pulmonary nodules using the open-source 3D Slicer software⁶ and the Chest Imaging Platform (CIP) extension⁷. The Lung Lesion Analyzer (LLA) module within CIP was used for nodule segmentations. The semi-automated segmentation algorithm has been previously validated against consensus segmentations performed manually by several trained radiologists and was found to perform similarly well⁸.

Technical details about the segmentation algorithm used in the LLA are described in⁹ and⁸. Here we provide a brief description of the algorithm. The segmentation algorithm used by the LLA is a level set algorithm⁹. The level set algorithm iteratively grows outward the boundary between the nodule and non-nodule, with the growth distance being proportional to the distance from the current front to a feature boundary⁹. These feature boundaries represent areas that the region growing algorithm should avoid. By default, the four feature boundaries are: (1) the lung wall, (2) the lung vasculature, (3) the boundary between the nodule and the background lung parenchyma, and (4) the low CT density of air. These boundaries allow the outward growth of the nodule segmentation, while deterring over-segmentation into the lung wall, vessel, or across sharp edges. In other words, the nodule segmentation iteratively grows, and the rate of growth slows down as the segmentation approaches parts of the lung that do not belong to the nodule. The boundary constraints improve upon other common segmentation algorithms, such as GrowCut, which can segment large tumor volumes with relative ease, but are less robust for smaller pulmonary lesions, such as those typically identified during lung cancer screening, or lesions with pleural and/or vessel attachments⁹.

1. **Lung wall** - The lung wall feature is used to deter the nodule contour from growing beyond the lung wall and into the pleura, which is especially important when segmenting juxtapleural lesions. The lung wall can be characterized by a much higher voxel intensity than the lung parenchyma (which is primarily air). However, juxtapleural lesions may have voxel intensities quite similar to the lung wall. These juxtapleural lesions create interruptions in the otherwise smooth, consistent curvature of the lung wall. Thus, the lung wall feature is created by first binarizing the image at a threshold of -400 HU, and then, for voxels near the lung boundary, apply a hole-filling algorithm at a per-voxel level to decide whether a given voxel will be filled based on a majority-voting scheme using a neighborhood of 7x7x7 surrounding the candidate voxel. The hole-filling algorithm is ran over many iterations until no voxels labels get changed from background to foreground. This has the effect of reducing surfaces to the point of having low Gaussian curvature. Lastly, a sigmoid function is applied to the final binary image to map the values to a smooth and continuous range.
2. **Vesselness** - Pulmonary nodules are compact in size, while lung vasculature and vessels are well-approximated by a cylinder or tube. This feature computes how closely a given image region resembles a tube. This is done using the Sato tubularness measure. A sigmoid function is applied to the final binary image.

3. **Gradient** - The gradient feature is used to help identify the edges of the lesion when the lesion is surrounded by a lower density structure/area, such as the lung parenchyma. The well-established Canny edge detector is used to produce an edge map. A sigmoid function is applied to the final binary image.
4. **Intensity** - The intensity feature is based on a simple intensity threshold. Based on whether the nodule is solid or part-solid, a threshold of -200 HU or -500 HU is used for thresholding, respectively. A sigmoid transformation is applied after thresholding.

All of the features are aggregated after normalizing each feature to have values in the range of [0,1] and the aggregated image is used for segmentation. The segmentation algorithm is initialized by the user placing a single seed point inside the nodule volume, typically at the 3D centroid of the nodule. The nodule segmentation is then performed using the above described level set algorithm, based on a front propagation approach⁹. The propagation of the segmentation is constrained to prevent leakage of the segmentation into non-nodule volumes including the chest wall, airway walls, or other regions with tubular or vessel-like structures⁹. After the segmentation algorithm is complete, the user may perform manual touch-ups to fix any over- or under-segmentations.

3 Ground-truth nodule malignancy status

Both the PanCan and IELCAP-Toronto tracked malignancy status (i.e. lung cancer) at a per-nodule level. However, for PLuSS and NLST, lung cancer status was only known at the patient level. Our radiomics feature extraction and analysis is at the nodule level, so we employed a set of heuristics to prepare these cohorts for inclusion in this study. For NLST and PLUSS, among participants with lung cancer and annotated nodules, we selected the nodule with the highest suspicion of malignancy for inclusion. Suspicion was determined (in order) by: (1) radiologist assigned LungRADS 1.1 score, (2) malignancy rating, (3) longest axis, and (4) longest perpendicular axis. We only included participants whose lung cancer diagnosis date was within 2 years of their baseline screen to avoid including lesions with low probability of being the lesion that led to a lung cancer diagnosis.

4 Initial filtering of radiomics features

We performed a first-pass filter of the radiomics features to reduce the set of predictors for inclusion in the cross-validation and machine learning model development. Next, we describe the reasoning and application of each of the filtering steps for preliminary feature selection. The filtering steps were applied in the order as shown.

1. Computational Issues

- First, we removed any predictors with zero-variance. In other words, predictors containing only a single unique value were removed as they would, by definition, have no predictive value in models due to lack of variability. Next, several variables were observed to be numerically unstable after applying some of the image filters (i.e., during feature extraction based on derived images). In particular, we removed the Coarseness (NGTDM) feature for all but the original and eight wavelet filters.

2. Weak Predictors

- We fit univariate logistic regression models for each of the radiomic features that passed Step 1, with nodule malignancy as the response variable. We removed putatively weak predictors based on the p-value associated with the beta coefficient (i.e., the logit) from the logistic regression model. We adjusted the p-values using the Benjamini-Hochberg correction to control the false-discovery rate (FDR)¹⁰. Any radiomic feature with a univariate FDR-adjusted p-value of less than 0.05 were retained.

3. Redundancy

- Lastly, we aimed to remove some of the redundancy among features due to extreme correlation. Several radiomic features are perfect correlates of one another and thus carry identical information for prediction purposes. We examined all pairwise sets of features with an absolute Pearson's correlation coefficient more than 0.9. We sorted the sets of predictors in descending order. Next, starting with the most highly correlated set of features, we removed one of the two features based on which features had the larger FDR-adjusted P-value. We iteratively performed this feature selection process until we had a pruned set of features with correlation of less than or equal to 0.9 (based on the absolute correlation).

There were also 1,284 pulmonary nodules excluded from our analytic sample due to technical issues with the feature extraction. Technical issues included: (1) missing or corrupt mask files (n=3), (2) issues with computing shape statistics (n=88), (3) geometric mismatches (n=93), (4) masks contained only a single voxel (n=448), (5) masks were 1-dimensional (n=540), or (6) removed nodules with sentinel values for incalculable features (n=112).

5 Application of the PanCan Model

The PanCan model is an established nodule malignancy model developed based on 1,871 participants from the PanCanadian Early Detection of Lung Cancer Study (PanCan)². The original paper describes four models, named as Model 1a (Parsimonious, No Spiculation), Model 2a (Full Model, No Spiculation), Model 1b (Parsimonious, with Spiculation), and Model 2b (Full Model, with Spiculation). The parsimonious models included sex (female vs. male), nodule size (mm), and nodule location (upper vs. middle or lower lobe). The full model further included age (years), family history of lung cancer (yes vs. no), emphysema (yes vs. no), nodule size (mm), nodule type (Nonsolid or with ground-glass opacity, Part-solid, Solid), and nodule count per scan (per additional nodule). Models 1a and 2a did not include spiculation (yes vs. no), while Models 1b and 2b included this variable. Nodule size is included in the models as a non-linear transformation based on multiple fractional polynomials. The functional form of nodule size (per mm) is as follows: $\left(\left(\frac{\text{Nodule size}}{10} \right)^{-0.5} \right) - 1.58113883$. Age was centered at 62 years, nodule size is centered at 4mm, and nodule count per scan was centered at 4 nodules.

We applied Model 2b (Full Model, with Spiculation) in our data set as this is the fullest model containing all of the predictors. Since the PanCan Model was developed in PanCan, we only apply the PanCan Model to the NLST, IELCAP-Toronto, and PLuSS to avoid presenting overly-optimistic performance metrics. The risk formula for the PanCan Models is:

$$\begin{aligned} \text{PanCan Logit} = & -6.7892 + ((\text{Age} - 62) * 0.0287) + (\text{Female} * 0.6011) + (\text{FHLC} * 0.2961) + \\ & (\text{COPD} * 0.2953) + \left(\left(\left(\frac{\text{Nodule size}}{10} \right)^{-0.5} \right) - 1.58113883 \right) * -5.3854 \Big) + \\ & (\text{GGO} * -0.1276) + (\text{Part solid} * 0.3770) + (\text{Upper lobe} * 0.6581) + \\ & ((\text{Nodule count} - 4) * -0.0824) + (\text{Spiculation} * 0.7729) \end{aligned}$$

Where Female, FHLC, COPD, GGO, Part Solid, Upper Lobe, and Spiculation are binary indicator variables for the presence (1) or absence (0) of the trait. We can then get the probability as:

$$\text{PanCan Prob} = \frac{\exp(\text{PanCan Logit})}{(1 + \text{PanCan Logit})}$$

References

1. Team NLSTR: The national lung screening trial: Overview and study design. *Radiology* 258:243–253, 2011
2. McWilliams A, Tammemagi MC, Mayo JR, et al: Probability of cancer in pulmonary nodules detected on first screening CT. *New England Journal of Medicine* 369:910–919, 2013
3. Tammemagi MC, Schmidt H, Martel S, et al: Participant selection for lung cancer screening by risk modelling (the pan-canadian early detection of lung cancer [PanCan] study): A single-arm, prospective study. *The lancet oncology* 18:1523–1531, 2017
4. Roberts HC, Patsios D, Paul NS, et al: Lung cancer screening with low-dose computed tomography: Canadian experience. *Canadian Association of Radiologists Journal* 58:225, 2007
5. Wilson DO, Weissfeld JL, Fuhrman CR, et al: The pittsburgh lung screening study (PLuSS) outcomes within 3 years of a first computed tomography scan. *American journal of respiratory and critical care medicine* 178:956–961, 2008
6. Fedorov A, Beichel R, Kalpathy-Cramer J, et al: 3D slicer as an image computing platform for the quantitative imaging network. *Magnetic resonance imaging* 30:1323–1341, 2012
7. San Jose Estepar R, Ross JC, Harmouche R, et al: Chest imaging platform: An open-source library and workstation for quantitative chest imaging, in C66. Lung imaging II: New probes and emerging technologies. American Thoracic Society, 2015, pp A4975–A4975
8. Yip SS, Parmar C, Blezek D, et al: Application of the 3D slicer chest imaging platform segmentation algorithm for large lung nodule delineation. *PLoS One* 12:e0178944, 2017
9. Krishnan K, Ibanez L, Turner WD, et al: An open-source toolkit for the volumetric measurement of CT lung lesions. *Optics Express* 18:15256–15266, 2010
10. Benjamini Y, Hochberg Y: Controlling the false discovery rate: A practical and powerful approach to multiple testing. *Journal of the Royal statistical society: series B (Methodological)* 57:289–300, 1995

Supplemental Table 1. Ratings systems used for collecting semantic nodule features for IELCAP-Toronto, PanCan, and PLuSS.

Feature	Rating System					
Calcification	1=popcorn	2=laminated	3=solid	4=non-central	5=central	6=absent
Internal structure	Soft tissue	Fluid	Fat	Air		
Lobulation	1=none	2	3	4	5=marked	
Malignancy	1=highly unlikely	2=moderately unlikely	3=indeterminate	4=moderately suspicious	5=highly suspicious	
Margin	1=poorly defined	2	3	4	5=sharp	
Radiographic solidity	1=non-solid/GGO	2	3=part-solid/mixed	4	5=solid	
Sphericity	1=linear	2	3=ovoid	4	5=round	
Subtlety	1=extremely subtle	2=moderately subtle	3=fairly subtle	4=moderately obvious	5=obvious	
Spiculation	1=none	2	3	4	5=marked	

Note: The rating system was based on the semantic features described in The Lung Image Database Consortium (LIDC) Data Collection Process for Nodule Detection and Annotation; McNitt-Gray MF, Armato III SG, Meyer CR, Reeves AP, McLennan G, Pais RC, Freymann J, Brown MS, Engelmann RM, Bland PH, Laderach GE. The Lung Image Database Consortium (LIDC) data collection process for nodule detection and annotation. Academic radiology. 2007 Dec 1;14(12):1464-74.

Supplemental Table 2. Radiomic features extracted based on the PyRadiomics library.

First-order statistics	Shaped-based (3D)	Gray level cooccurrence matrix	Gray level size zone matrix	Gray level run length matrix	Neighbouring gray tone difference matrix	Gray level dependence matrix
Energy	Mesh volume	Autocorrelation	Small Area Emphasis (SAE)	Short Run Emphasis (SRE)	Coarseness	Small Dependence Emphasis (SDE)
Total Energy	Voxel volume	Joint Average	Large Area Emphasis (LAE)	Long Run Emphasis (LRE)	Contrast	Large Dependence Emphasis (LDE)
Entropy	Surface Area	Cluster Prominence	Gray Level Non-Uniformity (GLN)	Gray Level Non-Uniformity (GLN)	Busyness	Gray Level Non-Uniformity (GLN)
Minimum	Surface area to volume ratio	Cluster Shade	Gray Level Non-Uniformity Normalized (GLNN)	Gray Level Non-Uniformity Normalized (GLNN)	Complexity	Dependence Non-Uniformity (DN)
10 th percentile	Sphericity	Cluster Tendency	Size-Zone Non-Uniformity (SZN)	Run Length Non-Uniformity (RLN)	Strength	Dependence Non-Uniformity Normalized (DNN)
90 th percentile	Maximum 3D diameter	Contrast	Size-Zone Non-Uniformity Normalized (SZNN)	Run Length Non-Uniformity Normalized (RLNN)		Gray Level Variance (GLV)
Maximum	Maximum 2D diameter (Slice)	Correlation	Zone Percentage (ZP)	Run Percentage (RP)		Dependence Variance (DV)
Mean	Maximum 2D diameter (Column)	Difference Average	Gray Level Variance (GLV)	Gray Level Variance (GLV)		Dependence Entropy (DE)
Median	Maximum 2D diameter (Row)	Difference Entropy	Zone Variance (ZV)	Run Variance (RV)		Low Gray Level Emphasis (LGLE)
Interquartile range	Major axis length	Difference Variance	Zone Entropy (ZE)	Run Entropy (RE)		High Gray Level Emphasis (HGLE)
Range	Minor axis length	Joint Energy	Low Gray Level Zone Emphasis (LGLZE)	Low Gray Level Run Emphasis (LGLRE)		Small Dependence Emphasis (SDLGLE)
Mean absolute deviation (MAD)	Least axis length	Joint Entropy	High Gray Level Zone Emphasis (HGLZE)	High Gray Level Run Emphasis (HGLRE)		Small Dependence High Gray Level Emphasis (SDHGLE)
Robust mean absolute deviation (rMAD)	Elongation	Informational Measure of Correlation (IMC) 1	Small Area Low Gray Level Emphases (SALGLE)	Small Run Low Gray Level Emphases (SRLGLE)		Large Dependence Low Gray Level Emphasis (LDLGLE)
Root mean squared (RMS)	Flatness	Informational Measure of Correlation (IMC) 2	Small Area High Gray Level Emphasis (SAHGLE)	Small Run High Gray Level Emphasis (SRHGLE)		Large Dependence High Gray Level Emphasis (LDHGLE)
Skewness		Inverse Difference Moment (IDM)	Large Area Low Gray Level Emphasis (LALGLE)	Large Run Low Gray Level Emphasis (LRLGLE)		

Kurtosis	Maximal Correlation Coefficient (MCC)	Large Area High Gray Level Emphasis (LAHGLE)	Large Run High Gray Level Emphasis (LRHGLE)
Variance	Inverse Difference Moment Normalized (IDMN)		
Uniformity	Inverse Difference (ID) Inverse Difference Normalized (IDN) Inverse Variance Maximum Probability Sum Average Sum Entropy Sum of Squares		

Supplemental Table 3. Patient-level descriptive statistics for the training and testing splits used in this study. Means and standard deviations are reported for numeric variables and counts and proportions are reported for categorical variables.

	Total Participants (N = 6,865)	
	Training (80%) (n = 5,546)	Testing (20%) (n = 1,319)
No. lung cancers (%)	349 (6.3%)	90 (6.8%)
Age (years)	62.4 [6.0]	62.4 [5.9]
Sex		
Male	3,031 (54.6%)	711 (53.9%)
Female	2,535 (45.7%)	908 (46.1%)
Body mass index (kg/m ²)	27.3 [4.9]	27.2 [4.8]
Family history of lung cancer		
No	4,254 (76.7%)	1,006 (76.3%)
Yes	1,292 (23.3%)	313 (23.7%)
History of COPD or Emphysema		
No	4,756 (85.8%)	1,142 (86.6%)
Yes	790 (14.2%)	177 (13.4%)
Smoking status		
Current	2,912 (52.5%)	712 (54.0%)
Former	2634 47.5	607 46.0
Years smoked	40.4 [8.8]	41.0 [8.1]
Cigarettes per day	26.7 [11.3]	26.0 [10.4]
Years since cessation	27.2 [16.4]	27.3 [16.8]
Nodules per participant	5.02 [4.5]	6.00 [5.6]

Abbreviations: COPD, chronic obstructive pulmonary disease; IELCAP, International Early Lung Cancer Action Plan; mm, millimeter; NLST, National Lung Screening Trial; No., number; PanCan, PanCanadian Early Detection of Lung Cancer Study; PLuSS, Pittsburgh Lung Screening Study.

Supplemental Table 4. Nodule-level descriptive statistics for the training and testing splits used in this study. Means and standard deviations are reported for numeric variables and counts and proportions are reported for categorical variables.

	Training (80%) (N = 13,434)		Testing (20%) (N = 3,363)	
	Benign (n = 13,028)	Malignant (N = 406)	Benign (N = 3,256)	Malignant (N = 107)
Time to diagnosis (days)				
Mean [SD]	–	278 [304]	–	276 [308]
Median [IQR]	–	132 [390]	–	136 [396]
Nodule solidity				
Solid	9,722 (80.4%)	292 (73.9%)	2,336 (78.4%)	75 (71.4%)
Subsolid	2,366 (19.6%)	103 (26.1%)	643 (21.66%)	30 (28.6%)
Nodule location				
Left lower lobe	2,465 (19.2%)	49 (12.3%)	590 (18.3%)	14 (13.3%)
Left upper lobe	2,609 (20.4%)	112 (28.2%)	638 (19.8%)	23 (21.9%)
Right lower lobe	2,777 (21.7%)	76 (19.1%)	718 (22.3%)	24 (22.9%)
Right middle lobe	1,530 (11.9%)	20 (5.0%)	375 (11.7%)	5 (4.8%)
Right upper lobe	3,430 (26.8%)	140 (35.3%)	897 (27.9%)	39 (37.1%)
Major axis length (mm)	7.82 [6.54]	21.77 [14.19]	7.66 [5.98]	21.69 [13.02]
Minor axis length (mm)	5.51 [4.00]	16.19 [10.30]	5.41 [3.76]	16.44 [9.93]
Least axis length (mm)	3.99 [2.91]	12.61 [8.00]	3.89 [2.77]	12.92 [8.13]
Mesh Volume (mm ³)	328.3 [1854.4]	6706.0 [19087.4]	282.7 [1313.6]	6651.6 [18420.9]
Surface Area (mm ²)	231.3 [618.4]	2196.3 [3625.0]	217.0 [547.8]	2141.1 [3029.4]
SA to Volume Ratio	1.94 [1.11]	0.77 [0.42]	1.96 [1.10]	0.74 [0.41]
Flatness	0.52 [0.18]	0.61 [0.13]	0.51 [0.18]	0.61 [0.13]
Elongation	0.73 [0.15]	0.77 [0.13]	0.73 [0.15]	0.77 [0.13]
Sphericity	0.77 [0.09]	0.64 [0.11]	0.77 [0.09]	0.65 [0.10]

Abbreviations: IQR, interquartile range; mm, millimeter; SA, surface area; SD, standard deviation.

Supplemental Table 5. Descriptive statistics for the distribution of radiomic features across all four lung cancer screening studies.

Feature	Mean	SD	Q25	Median	Q75	Min	Max
First Order							
10Percentile	-578.30	189.20	-737.10	-599.84	-435.40	-1783.00	813.90
90Percentile	-146.79	327.52	-348.70	-141.20	14.00	-1036.30	2235.00
Energy	342222389.86	3569036686.6	7171515.00	24780211.00	77743212.00	182154.00	24924111152
		7					9.92
Entropy	3.90	1.02	3.21	4.12	4.70	0.57	6.87
InterquartileRange	247.27	157.24	137.95	225.50	321.00	0.00	1814.25
Kurtosis	2.52	1.26	2.01	2.28	2.69	1.00	50.66
Maximum	-5.73	404.09	-232.00	-17.00	127.60	-841.62	3006.00
Mean	-366.85	233.17	-537.80	-364.72	-224.57	-1468.31	1165.78
MeanAbsoluteDeviation	141.91	84.85	85.88	131.07	178.43	6.15	907.36
Median	-372.63	237.70	-558.00	-372.00	-215.50	-1515.50	1423.00
Minimum	-698.77	200.11	-852.00	-739.00	-549.00	-3024.00	783.00
Range	693.05	422.36	400.00	646.00	889.00	23.00	3843.00
RobustMeanAbsoluteDeviation	101.34	65.66	57.38	93.65	132.36	0.00	756.97
RootMeanSquared	659.74	243.37	490.53	662.72	798.61	97.73	2364.31
Skewness	0.11	0.57	-0.21	0.13	0.45	-6.04	4.32
TotalEnergy	342237726.54	3569035354.2	7190243.00	24798216.00	77772859.00	182154.00	24924111152
		6					9.92
Uniformity	0.10	0.08	0.04	0.07	0.12	0.01	0.81
Variance	39243.61	64258.38	10959.85	25036.20	45340.70	62.85	1017823.06
Gray Level Co-occurrence Matrix (GLCM)							
Autocorrelation	331.99	420.22	78.36	215.07	443.75	1.17	12595.05
ClusterProminence	189793.50	1208786.45	2302.68	19723.28	82202.64	0.00	40054589.22
ClusterShade	133.85	4914.62	-266.72	-3.67	69.64	-202132.69	138982.72
ClusterTendency	141.10	236.69	28.09	84.36	178.03	0.00	3926.45
Contrast	98.68	212.14	28.18	53.48	92.44	0.17	3891.90
Correlation	0.11	0.42	-0.14	0.19	0.43	-1.00	0.94
DifferenceAverage	6.62	4.48	4.22	5.84	7.70	0.17	49.15
DifferenceEntropy	2.85	1.28	2.04	3.27	3.80	0.00	5.97
DifferenceVariance	28.88	64.37	6.85	16.09	28.78	0.00	1262.46
Id	0.26	0.09	0.21	0.25	0.30	0.03	0.92
Idm	0.18	0.10	0.12	0.16	0.21	0.00	0.92
Idmn	0.92	0.06	0.89	0.93	0.95	0.60	1.00
Idn	0.82	0.06	0.78	0.83	0.86	0.55	0.98
Imc1	-0.57	0.26	-0.80	-0.57	-0.36	-1.00	-0.01
Imc2	0.95	0.07	0.94	0.98	1.00	0.15	1.00
InverseVariance	0.18	0.10	0.12	0.16	0.22	0.00	1.00
JointAverage	15.56	8.80	8.89	14.39	20.54	1.08	111.61
JointEnergy	0.09	0.15	0.01	0.02	0.10	0.00	0.80
JointEntropy	5.38	2.39	3.44	5.81	7.28	0.40	12.22
MaximumProbability	0.84	0.15	0.72	0.88	1.00	0.10	1.00

MCC	0.11	0.14	0.02	0.04	0.13	0.00	0.83
SumAverage	31.12	17.60	17.78	28.78	41.08	2.17	223.23
SumEntropy	3.66	1.79	2.33	4.18	5.12	0.00	7.81
SumSquares	59.94	105.08	16.18	37.38	67.72	0.07	1549.00
Gray Level Dependence Matrix (GLDM)							
DependenceEntropy	4.74	1.51	3.62	5.01	5.91	0.81	8.31
DependenceNonUniformity	103.57	555.67	9.33	26.40	65.60	1.67	35608.44
DependenceNonUniformityNormalized	0.44	0.22	0.30	0.38	0.52	0.04	1.00
DependenceVariance	1.48	3.16	0.27	0.72	1.35	0.00	61.12
GrayLevelNonUniformity	41.78	728.25	1.91	4.29	9.58	1.00	69111.30
GrayLevelVariance	62.86	102.79	17.60	40.13	72.63	0.10	1628.29
HighGrayLevelEmphasis	330.94	416.98	87.78	213.50	427.63	1.43	10962.68
LargeDependenceEmphasis	5.95	9.08	2.43	3.81	5.88	1.00	227.44
LargeDependenceHighGrayLevelEmphasis	2919.93	10415.08	321.75	890.24	2011.22	3.00	364026.71
LargeDependenceLowGrayLevelEmphasis	0.25	0.91	0.04	0.09	0.21	0.00	50.31
LowGrayLevelEmphasis	0.08	0.10	0.02	0.04	0.10	0.00	0.89
SmallDependenceEmphasis	0.59	0.20	0.47	0.58	0.71	0.02	1.00
SmallDependenceHighGrayLevelEmphasis	189.25	318.54	46.99	114.11	215.81	0.11	7085.44
SmallDependenceLowGrayLevelEmphasis	0.06	0.08	0.01	0.03	0.08	0.00	0.57
Gray Level Run Length Matrix (GLRLM)							
GrayLevelNonUniformity	28.92	375.87	1.85	4.13	9.08	1.00	33004.92
GrayLevelNonUniformityNormalized	0.10	0.08	0.04	0.07	0.12	0.01	0.74
GrayLevelVariance	62.99	102.84	17.76	40.39	72.58	0.15	1628.00
HighGrayLevelRunEmphasis	327.99	414.23	87.80	212.85	423.01	1.54	10954.98
LongRunEmphasis	1.15	1.15	1.06	1.10	1.15	1.00	147.39
LongRunHighGrayLevelEmphasis	386.00	512.17	98.66	235.67	480.35	2.36	12031.22
LongRunLowGrayLevelEmphasis	0.09	0.14	0.02	0.04	0.11	0.00	10.00
LowGrayLevelRunEmphasis	0.08	0.10	0.02	0.04	0.10	0.00	0.86
RunEntropy	4.04	1.06	3.34	4.26	4.87	0.92	7.02
RunLengthNonUniformity	381.19	2310.97	17.33	65.28	177.17	2.00	124834.97
RunLengthNonUniformityNormalized	0.93	0.05	0.91	0.94	0.96	0.42	1.00
RunPercentage	0.96	0.03	0.95	0.97	0.98	0.52	1.00
RunVariance	0.05	0.39	0.02	0.03	0.05	0.00	49.00
ShortRunEmphasis	0.97	0.03	0.96	0.98	0.99	0.65	1.00
ShortRunHighGrayLevelEmphasis	317.03	404.33	85.34	207.11	409.83	1.34	10694.45
ShortRunLowGrayLevelEmphasis	0.08	0.09	0.02	0.04	0.10	0.00	0.66
Gray Level Size Zone Matrix (GLSZM)							
GrayLevelNonUniformity	7.63	32.08	1.33	2.62	5.10	1.00	1603.45
GrayLevelNonUniformityNormalized	0.09	0.08	0.04	0.06	0.11	0.01	0.56
GrayLevelVariance	64.02	103.39	19.91	42.00	71.52	0.22	1654.18
HighGrayLevelZoneEmphasis	302.91	394.91	87.50	202.30	380.20	2.00	10976.70
LargeAreaEmphasis	242.78	10666.83	1.88	3.00	5.44	1.00	1226672.91
LargeAreaHighGrayLevelEmphasis	348968.57	17648745.70	273.00	763.88	1870.58	3.00	2067360221.7

LargeAreaLowGrayLevelEmphasis	1.48	63.16	0.05	0.10	0.24	0.00	7771.40
LowGrayLevelZoneEmphasis	0.09	0.10	0.02	0.05	0.12	0.00	0.75
SizeZoneNonUniformity	96.54	507.46	8.20	23.94	60.58	1.00	30043.86
SizeZoneNonUniformityNormalized	0.58	0.18	0.47	0.56	0.68	0.06	1.00
SmallAreaEmphasis	0.77	0.13	0.70	0.77	0.84	0.02	1.00
SmallAreaHighGrayLevelEmphasis	235.76	351.72	63.16	148.93	280.09	0.16	8710.21
SmallAreaLowGrayLevelEmphasis	0.08	0.09	0.02	0.04	0.10	0.00	0.68
ZoneEntropy	4.52	1.36	3.55	4.76	5.57	0.92	7.90
ZonePercentage	0.67	0.19	0.57	0.68	0.80	0.01	1.00
ZoneVariance	236.47	10641.88	0.24	0.78	2.24	0.00	1226340.91
Neighbouring Gray Tone Difference Matrix (NGTDM)							
Busyness	0.18	0.34	0.06	0.10	0.19	0.00	14.98
Coarseness	0.09	0.11	0.03	0.06	0.12	0.00	1.50
Complexity	1859.31	5011.82	243.90	850.51	1871.17	0.22	173314.58
Contrast	11.71	132.30	0.37	0.64	1.59	0.01	8884.17
Strength	16.05	16.10	7.00	12.41	19.69	0.03	187.81
Shape (3D)							
Elongation	0.73	0.15	0.63	0.74	0.84	0.02	1.00
Flatness	0.52	0.18	0.43	0.54	0.64	0.00	1.00
LeastAxisLength	4.23	3.50	2.06	3.61	5.24	0.00	51.43
MajorAxisLength	8.22	7.20	4.18	6.55	9.40	2.00	250.32
Maximum2DDiameterColumn	8.45	7.62	4.12	6.71	10.00	1.00	259.01
Maximum2DDiameterRow	8.40	7.45	4.12	6.71	10.00	1.00	259.02
Maximum2DDiameterSlice	8.05	6.96	4.12	6.32	9.22	1.00	110.55
Maximum3DDiameter	9.69	8.74	4.58	7.81	11.18	2.24	259.03
MeshVolume	513.89	3889.98	14.79	66.29	191.17	0.83	237030.42
MinorAxisLength	5.82	4.66	2.97	4.84	6.82	0.83	77.13
Sphericity	0.77	0.09	0.72	0.78	0.83	0.13	0.94
SurfaceArea	288.16	918.09	35.68	102.58	215.23	6.22	31775.90
SurfaceVolumeRatio	1.91	1.11	1.13	1.55	2.45	0.13	8.80
VoxelVolume	522.67	3895.85	18.00	73.00	201.00	2.06	237180.00

Abbreviations: P25, 25th percentile; P75, 75th percentile; SD, standard deviation.

Supplemental Table 6. Set of 642 radiomics features retained after the filtering steps described in the Supplementary Methods and in Supplemental Figure 2.

Class	Features
First Order	original_firstorder_10Percentile, original_firstorder_Kurtosis, original_firstorder_Maximum, original_firstorder_MeanAbsoluteDeviation, original_firstorder_Mean, original_firstorder_Minimum, original_firstorder_Range, original_firstorder_Skewness, wavelet-LLH_firstorder_10Percentile, wavelet-LLH_firstorder_Maximum, wavelet-LLH_firstorder_MeanAbsoluteDeviation, wavelet-LLH_firstorder_Mean, wavelet-LHL_firstorder_10Percentile, wavelet-LHL_firstorder_Kurtosis, wavelet-LHL_firstorder_Maximum, wavelet-LHL_firstorder_MeanAbsoluteDeviation, wavelet-LHL_firstorder_Mean, wavelet-LHL_firstorder_Minimum, wavelet-LHL_firstorder_Range, wavelet-LHL_firstorder_Skewness, wavelet-LHH_firstorder_10Percentile, wavelet-LHH_firstorder_Maximum, wavelet-LHH_firstorder_MeanAbsoluteDeviation, wavelet-LHH_firstorder_Mean, wavelet-LHH_firstorder_Minimum, wavelet-LHH_firstorder_Range, wavelet-HLL_firstorder_10Percentile, wavelet-HLL_firstorder_Kurtosis, wavelet-HLL_firstorder_Maximum, wavelet-HLL_firstorder_MeanAbsoluteDeviation, wavelet-HLL_firstorder_Mean, wavelet-HLL_firstorder_Minimum, wavelet-HLL_firstorder_Range, wavelet-HLL_firstorder_Skewness, wavelet-HLH_firstorder_10Percentile, wavelet-HLH_firstorder_Kurtosis, wavelet-HLH_firstorder_Maximum, wavelet-HLH_firstorder_MeanAbsoluteDeviation, wavelet-HLH_firstorder_Minimum, wavelet-HLH_firstorder_Range, wavelet-HHL_firstorder_Kurtosis, wavelet-HHL_firstorder_Maximum, wavelet-HHL_firstorder_MeanAbsoluteDeviation, wavelet-HHL_firstorder_Mean, wavelet-HHL_firstorder_Minimum, wavelet-HHL_firstorder_Range, wavelet-HHH_firstorder_10Percentile, wavelet-HHH_firstorder_Maximum, wavelet-HHH_firstorder_MeanAbsoluteDeviation, wavelet-HHH_firstorder_Minimum, wavelet-HHH_firstorder_Range, wavelet-LLL_firstorder_10Percentile, wavelet-LLL_firstorder_Kurtosis, wavelet-LLL_firstorder_Maximum, wavelet-LLL_firstorder_MeanAbsoluteDeviation, wavelet-LLL_firstorder_Mean, wavelet-LLL_firstorder_Minimum, wavelet-LLL_firstorder_Range, wavelet-LLL_firstorder_Skewness, log-sigma-1-0-mm-3D_firstorder_10Percentile, log-sigma-1-0-mm-3D_firstorder_Kurtosis, log-sigma-1-0-mm-3D_firstorder_Maximum, log-sigma-1-0-mm-3D_firstorder_MeanAbsoluteDeviation, log-sigma-1-0-mm-3D_firstorder_Mean, log-sigma-1-0-mm-3D_firstorder_Minimum, log-sigma-1-0-mm-3D_firstorder_Range, log-sigma-2-0-mm-3D_firstorder_10Percentile, log-sigma-2-0-mm-3D_firstorder_Kurtosis, log-sigma-2-0-mm-3D_firstorder_Maximum, log-sigma-2-0-mm-3D_firstorder_MeanAbsoluteDeviation, log-sigma-2-0-mm-3D_firstorder_Minimum, log-sigma-2-0-mm-3D_firstorder_Range, log-sigma-2-0-mm-3D_firstorder_Skewness, log-sigma-3-0-mm-3D_firstorder_10Percentile, log-sigma-3-0-mm-3D_firstorder_Kurtosis, log-sigma-3-0-mm-3D_firstorder_Maximum, log-sigma-3-0-mm-3D_firstorder_MeanAbsoluteDeviation, log-sigma-3-0-mm-3D_firstorder_Mean, log-sigma-3-0-mm-3D_firstorder_Minimum, log-sigma-3-0-mm-3D_firstorder_Range, log-sigma-3-0-mm-3D_firstorder_Skewness, log-sigma-4-0-mm-3D_firstorder_10Percentile, log-sigma-4-0-mm-3D_firstorder_Kurtosis, log-sigma-4-0-mm-3D_firstorder_Maximum, log-sigma-4-0-mm-3D_firstorder_MeanAbsoluteDeviation, log-sigma-4-0-mm-3D_firstorder_Mean, log-sigma-4-0-mm-3D_firstorder_Minimum, log-sigma-4-0-mm-3D_firstorder_Range, log-sigma-5-0-mm-3D_firstorder_10Percentile, log-sigma-5-0-mm-3D_firstorder_MeanAbsoluteDeviation, log-sigma-5-0-mm-3D_firstorder_Mean, log-sigma-5-0-mm-3D_firstorder_Minimum, log-sigma-5-0-mm-3D_firstorder_Range, log-sigma-5-0-mm-3D_firstorder_Skewness, square_firstorder_10Percentile, square_firstorder_Kurtosis, square_firstorder_Maximum, square_firstorder_Mean, square_firstorder_Minimum, square_firstorder_Range, square_firstorder_Skewness, squareroot_firstorder_Kurtosis, squareroot_firstorder_Maximum, squareroot_firstorder_MeanAbsoluteDeviation, squareroot_firstorder_Mean, squareroot_firstorder_Minimum, squareroot_firstorder_Range, logarithm_firstorder_Kurtosis, logarithm_firstorder_Maximum, logarithm_firstorder_MeanAbsoluteDeviation, logarithm_firstorder_Mean, logarithm_firstorder_Minimum, logarithm_firstorder_Range, logarithm_firstorder_Skewness, exponential_firstorder_Kurtosis, exponential_firstorder_Maximum, exponential_firstorder_Mean, exponential_firstorder_Minimum, exponential_firstorder_Range, exponential_firstorder_Skewness, gradient_firstorder_10Percentile, gradient_firstorder_Kurtosis, gradient_firstorder_Maximum, gradient_firstorder_MeanAbsoluteDeviation, gradient_firstorder_Mean, gradient_firstorder_Minimum, gradient_firstorder_Range, gradient_firstorder_Skewness, lbp-3D-m1_firstorder_10Percentile, lbp-3D-m1_firstorder_Maximum, lbp-3D-m1_firstorder_MeanAbsoluteDeviation, lbp-3D-m1_firstorder_Mean, lbp-3D-m1_firstorder_Minimum, lbp-3D-m1_firstorder_Range, lbp-3D-m1_firstorder_Skewness, lbp-3D-m2_firstorder_10Percentile, lbp-3D-m2_firstorder_Maximum, lbp-3D-m2_firstorder_MeanAbsoluteDeviation, lbp-3D-m2_firstorder_Mean, lbp-3D-m2_firstorder_Minimum, lbp-3D-m2_firstorder_Range, lbp-3D-k_firstorder_10Percentile, lbp-3D-k_firstorder_Kurtosis, lbp-3D-k_firstorder_Maximum, lbp-3D-k_firstorder_MeanAbsoluteDeviation, lbp-3D-k_firstorder_Mean, lbp-3D-k_firstorder_Minimum, lbp-3D-k_firstorder_Range, lbp-3D-k_firstorder_Skewness

GLCM	<p>original_glcm_ClusterShade, original_glcm_ClusterTendency, original_glcm_DifferenceAverage, original_glcm_Idm, original_glcm_Idn, original_glcm_Imc1, original_glcm_Imc2, original_glcm_InverseVariance, original_glcm_MCC, wavelet-LLH_glcm_ClusterProminence, wavelet-LLH_glcm_ClusterTendency, wavelet-LLH_glcm_DifferenceAverage, wavelet-LLH_glcm_Idm, wavelet-LLH_glcm_Idn, wavelet-LLH_glcm_Imc1, wavelet-LLH_glcm_Imc2, wavelet-LLH_glcm_InverseVariance, wavelet-LLH_glcm_MCC, wavelet-LHL_glcm_ClusterProminence, wavelet-LHL_glcm_ClusterTendency, wavelet-LHL_glcm_DifferenceAverage, wavelet-LHL_glcm_Idm, wavelet-LHL_glcm_Idn, wavelet-LHL_glcm_Imc1, wavelet-LHL_glcm_Imc2, wavelet-LHL_glcm_InverseVariance, wavelet-LHL_glcm_MCC, wavelet-LHH_glcm_ClusterTendency, wavelet-LHH_glcm_DifferenceAverage, wavelet-LHH_glcm_Idm, wavelet-LHH_glcm_Idn, wavelet-LHH_glcm_Imc1, wavelet-LHH_glcm_Imc2, wavelet-LHH_glcm_InverseVariance, wavelet-LHH_glcm_MCC, wavelet-HLL_glcm_ClusterProminence, wavelet-HLL_glcm_ClusterTendency, wavelet-HLL_glcm_DifferenceAverage, wavelet-HLL_glcm_Idm, wavelet-HLL_glcm_Idn, wavelet-HLL_glcm_Imc1, wavelet-HLL_glcm_Imc2, wavelet-HLL_glcm_InverseVariance, wavelet-HLL_glcm_MCC, wavelet-HLH_glcm_ClusterProminence, wavelet-HLH_glcm_ClusterTendency, wavelet-HLH_glcm_DifferenceAverage, wavelet-HLH_glcm_Idm, wavelet-HLH_glcm_Idn, wavelet-HLH_glcm_Imc1, wavelet-HLH_glcm_Imc2, wavelet-HLH_glcm_InverseVariance, wavelet-HLH_glcm_MCC, wavelet-HHL_glcm_DifferenceAverage, wavelet-HHL_glcm_Idm, wavelet-HHL_glcm_Idn, wavelet-HHL_glcm_Imc1, wavelet-HHL_glcm_Imc2, wavelet-HHL_glcm_InverseVariance, wavelet-HHL_glcm_MCC, wavelet-HHH_glcm_DifferenceAverage, wavelet-HHH_glcm_Idm, wavelet-HHH_glcm_Idn, wavelet-HHH_glcm_Imc1, wavelet-HHH_glcm_Imc2, wavelet-HHH_glcm_InverseVariance, wavelet-HHH_glcm_MCC, wavelet-LLL_glcm_ClusterShade, wavelet-LLL_glcm_ClusterTendency, wavelet-LLL_glcm_DifferenceAverage, wavelet-LLL_glcm_Idm, wavelet-LLL_glcm_Idn, wavelet-LLL_glcm_Imc1, wavelet-LLL_glcm_Imc2, wavelet-LLL_glcm_InverseVariance, wavelet-LLL_glcm_MCC, log-sigma-1-0-mm-3D_glcm_DifferenceAverage, log-sigma-1-0-mm-3D_glcm_Idm, log-sigma-1-0-mm-3D_glcm_Idn, log-sigma-1-0-mm-3D_glcm_Imc1, log-sigma-1-0-mm-3D_glcm_Imc2, log-sigma-1-0-mm-3D_glcm_InverseVariance, log-sigma-1-0-mm-3D_glcm_MCC, log-sigma-2-0-mm-3D_glcm_ClusterTendency, log-sigma-2-0-mm-3D_glcm_Idn, log-sigma-2-0-mm-3D_glcm_Imc1, log-sigma-2-0-mm-3D_glcm_Imc2, log-sigma-3-0-mm-3D_glcm_ClusterProminence, log-sigma-3-0-mm-3D_glcm_ClusterTendency, log-sigma-3-0-mm-3D_glcm_DifferenceAverage, log-sigma-3-0-mm-3D_glcm_Idm, log-sigma-3-0-mm-3D_glcm_Idn, log-sigma-3-0-mm-3D_glcm_Imc1, log-sigma-3-0-mm-3D_glcm_Imc2, log-sigma-3-0-mm-3D_glcm_InverseVariance, log-sigma-3-0-mm-3D_glcm_MCC, log-sigma-4-0-mm-3D_glcm_ClusterProminence, log-sigma-4-0-mm-3D_glcm_ClusterShade, log-sigma-4-0-mm-3D_glcm_ClusterTendency, log-sigma-4-0-mm-3D_glcm_DifferenceAverage, log-sigma-4-0-mm-3D_glcm_Idm, log-sigma-4-0-mm-3D_glcm_Idn, log-sigma-4-0-mm-3D_glcm_Imc1, log-sigma-4-0-mm-3D_glcm_Imc2, log-sigma-4-0-mm-3D_glcm_InverseVariance, log-sigma-4-0-mm-3D_glcm_MCC, log-sigma-5-0-mm-3D_glcm_ClusterProminence, log-sigma-5-0-mm-3D_glcm_ClusterShade, log-sigma-5-0-mm-3D_glcm_ClusterTendency, log-sigma-5-0-mm-3D_glcm_DifferenceAverage, log-sigma-5-0-mm-3D_glcm_Idm, log-sigma-5-0-mm-3D_glcm_Idn, log-sigma-5-0-mm-3D_glcm_Imc1, log-sigma-5-0-mm-3D_glcm_Imc2, log-sigma-5-0-mm-3D_glcm_InverseVariance, log-sigma-5-0-mm-3D_glcm_MCC, square_glcm_DifferenceAverage, square_glcm_Idm, square_glcm_Idn, square_glcm_Imc1, square_glcm_Imc2, square_glcm_InverseVariance, square_glcm_MCC, squareroot_glcm_ClusterTendency, squareroot_glcm_DifferenceAverage, squareroot_glcm_Idn, squareroot_glcm_Imc1, squareroot_glcm_Imc2, squareroot_glcm_MCC, logarithm_glcm_ClusterProminence, logarithm_glcm_ClusterTendency, logarithm_glcm_Idm, logarithm_glcm_Idn, logarithm_glcm_Imc1, logarithm_glcm_InverseVariance, logarithm_glcm_MCC, exponential_glcm_Imc1, exponential_glcm_Imc2, exponential_glcm_InverseVariance, gradient_glcm_ClusterShade, gradient_glcm_ClusterTendency, gradient_glcm_DifferenceAverage, gradient_glcm_Idm, gradient_glcm_Idn, gradient_glcm_Imc1, gradient_glcm_Imc2, gradient_glcm_InverseVariance, gradient_glcm_MCC, lbp-3D-k_glcm_ClusterProminence, lbp-3D-k_glcm_ClusterShade, lbp-3D-k_glcm_ClusterTendency, lbp-3D-k_glcm_DifferenceAverage, lbp-3D-k_glcm_Idm, lbp-3D-k_glcm_Idn, lbp-3D-k_glcm_Imc1, lbp-3D-k_glcm_InverseVariance, lbp-3D-k_glcm_MCC</p>
GLDM	<p>original_gldm_DependenceNonUniformityNormalized, original_gldm_LargeDependenceEmphasis, original_gldm_LargeDependenceHighGrayLevelEmphasis, original_gldm_LargeDependenceLowGrayLevelEmphasis, wavelet-LLH_gldm_DependenceNonUniformityNormalized, wavelet-LLH_gldm_LargeDependenceEmphasis, wavelet-LLH_gldm_LargeDependenceHighGrayLevelEmphasis, wavelet-LHL_gldm_DependenceNonUniformityNormalized, wavelet-LHL_gldm_LargeDependenceEmphasis, wavelet-LHL_gldm_LargeDependenceHighGrayLevelEmphasis, wavelet-LHL_gldm_LargeDependenceLowGrayLevelEmphasis, wavelet-LHH_gldm_DependenceNonUniformityNormalized, wavelet-LHH_gldm_LargeDependenceEmphasis, wavelet-LHH_gldm_LargeDependenceHighGrayLevelEmphasis, wavelet-</p>

LHH_gldm_LargeDependenceLowGrayLevelEmphasis, wavelet-HLL_gldm_DependenceNonUniformityNormalized, wavelet-HLL_gldm_LargeDependenceEmphasis, wavelet-HLL_gldm_LargeDependenceHighGrayLevelEmphasis, wavelet-HLL_gldm_LargeDependenceLowGrayLevelEmphasis, wavelet-HLH_gldm_DependenceNonUniformityNormalized, wavelet-HLH_gldm_LargeDependenceEmphasis, wavelet-HLH_gldm_LargeDependenceHighGrayLevelEmphasis, wavelet-HHL_gldm_DependenceNonUniformityNormalized, wavelet-HHL_gldm_LargeDependenceEmphasis, wavelet-HHL_gldm_LargeDependenceHighGrayLevelEmphasis, wavelet-HHL_gldm_LargeDependenceLowGrayLevelEmphasis, wavelet-HHH_gldm_DependenceNonUniformityNormalized, wavelet-HHH_gldm_LargeDependenceEmphasis, wavelet-HHH_gldm_LargeDependenceHighGrayLevelEmphasis, wavelet-HHH_gldm_LargeDependenceLowGrayLevelEmphasis, wavelet-LLL_gldm_DependenceNonUniformityNormalized, wavelet-LLL_gldm_LargeDependenceEmphasis, wavelet-LLL_gldm_LargeDependenceHighGrayLevelEmphasis, wavelet-LLL_gldm_LargeDependenceLowGrayLevelEmphasis, log-sigma-1-0-mm-3D_gldm_DependenceNonUniformityNormalized, log-sigma-1-0-mm-3D_gldm_LargeDependenceEmphasis, log-sigma-1-0-mm-3D_gldm_LargeDependenceHighGrayLevelEmphasis, log-sigma-2-0-mm-3D_gldm_DependenceNonUniformityNormalized, log-sigma-2-0-mm-3D_gldm_LargeDependenceEmphasis, log-sigma-2-0-mm-3D_gldm_LargeDependenceHighGrayLevelEmphasis, log-sigma-2-0-mm-3D_gldm_LargeDependenceLowGrayLevelEmphasis, log-sigma-3-0-mm-3D_gldm_DependenceNonUniformityNormalized, log-sigma-3-0-mm-3D_gldm_LargeDependenceEmphasis, log-sigma-3-0-mm-3D_gldm_LargeDependenceHighGrayLevelEmphasis, log-sigma-3-0-mm-3D_gldm_LargeDependenceLowGrayLevelEmphasis, log-sigma-4-0-mm-3D_gldm_DependenceNonUniformityNormalized, log-sigma-4-0-mm-3D_gldm_LargeDependenceHighGrayLevelEmphasis, log-sigma-4-0-mm-3D_gldm_LargeDependenceLowGrayLevelEmphasis, log-sigma-5-0-mm-3D_gldm_DependenceNonUniformityNormalized, log-sigma-5-0-mm-3D_gldm_LargeDependenceHighGrayLevelEmphasis, log-sigma-5-0-mm-3D_gldm_LargeDependenceLowGrayLevelEmphasis, square_gldm_LargeDependenceEmphasis, square_gldm_LargeDependenceHighGrayLevelEmphasis, square_gldm_LargeDependenceLowGrayLevelEmphasis, squareroot_gldm_DependenceNonUniformityNormalized, squareroot_gldm_LargeDependenceEmphasis, squareroot_gldm_LargeDependenceHighGrayLevelEmphasis, logarithm_gldm_DependenceNonUniformityNormalized, logarithm_gldm_LargeDependenceEmphasis, logarithm_gldm_LargeDependenceHighGrayLevelEmphasis, logarithm_gldm_LargeDependenceLowGrayLevelEmphasis, exponential_gldm_LargeDependenceEmphasis, exponential_gldm_LargeDependenceHighGrayLevelEmphasis, exponential_gldm_LargeDependenceLowGrayLevelEmphasis, gradient_gldm_DependenceNonUniformityNormalized, gradient_gldm_LargeDependenceEmphasis, gradient_gldm_LargeDependenceHighGrayLevelEmphasis, gradient_gldm_LargeDependenceLowGrayLevelEmphasis, lbp-3D-m1_gldm_LargeDependenceEmphasis, lbp-3D-m1_gldm_LargeDependenceHighGrayLevelEmphasis, lbp-3D-m1_gldm_LargeDependenceLowGrayLevelEmphasis, lbp-3D-m2_gldm_LargeDependenceEmphasis, lbp-3D-m2_gldm_LargeDependenceHighGrayLevelEmphasis, lbp-3D-m2_gldm_LargeDependenceLowGrayLevelEmphasis, lbp-3D-k_gldm_DependenceNonUniformityNormalized, lbp-3D-k_gldm_LargeDependenceEmphasis, lbp-3D-k_gldm_LargeDependenceHighGrayLevelEmphasis, lbp-3D-k_gldm_LargeDependenceLowGrayLevelEmphasis

GLRLM

original_glrIm_GrayLevelNonUniformity, original_glrIm_LongRunLowGrayLevelEmphasis, original_glrIm_RunEntropy, original_glrIm_RunPercentage, original_glrIm_ShortRunLowGrayLevelEmphasis, wavelet-LLH_glrIm_GrayLevelNonUniformity, wavelet-LLH_glrIm_LongRunLowGrayLevelEmphasis, wavelet-LLH_glrIm_RunEntropy, wavelet-LLH_glrIm_RunPercentage, wavelet-LLH_glrIm_RunVariance, wavelet-LLH_glrIm_ShortRunLowGrayLevelEmphasis, wavelet-LHL_glrIm_GrayLevelNonUniformity, wavelet-LHL_glrIm_LongRunLowGrayLevelEmphasis, wavelet-LHL_glrIm_RunEntropy, wavelet-LHL_glrIm_RunPercentage, wavelet-LHL_glrIm_ShortRunLowGrayLevelEmphasis, wavelet-LHH_glrIm_GrayLevelNonUniformity, wavelet-LHH_glrIm_LongRunLowGrayLevelEmphasis, wavelet-LHH_glrIm_RunEntropy, wavelet-LHH_glrIm_RunPercentage, wavelet-LHH_glrIm_RunVariance, wavelet-LHH_glrIm_ShortRunLowGrayLevelEmphasis, wavelet-HLL_glrIm_GrayLevelNonUniformity, wavelet-HLL_glrIm_LongRunLowGrayLevelEmphasis, wavelet-HLL_glrIm_RunEntropy, wavelet-HLL_glrIm_RunPercentage, wavelet-HLL_glrIm_ShortRunLowGrayLevelEmphasis, wavelet-HLH_glrIm_GrayLevelNonUniformity, wavelet-HLH_glrIm_LongRunLowGrayLevelEmphasis, wavelet-HLH_glrIm_RunEntropy, wavelet-HLH_glrIm_RunPercentage, wavelet-HLH_glrIm_RunVariance, wavelet-HLH_glrIm_ShortRunLowGrayLevelEmphasis, wavelet-HHL_glrIm_GrayLevelNonUniformity, wavelet-HHL_glrIm_LongRunLowGrayLevelEmphasis, wavelet-HHL_glrIm_RunEntropy, wavelet-HHL_glrIm_RunPercentage, wavelet-

HHL_glrIm_ShortRunLowGrayLevelEmphasis, wavelet-HHH_glrIm_GrayLevelNonUniformity, wavelet-HHH_glrIm_LongRunLowGrayLevelEmphasis, wavelet-HHH_glrIm_RunEntropy, wavelet-HHH_glrIm_RunPercentage, wavelet-HHH_glrIm_RunVariance, wavelet-HHH_glrIm_ShortRunLowGrayLevelEmphasis, wavelet-LLL_glrIm_GrayLevelNonUniformity, wavelet-LLL_glrIm_LongRunLowGrayLevelEmphasis, wavelet-LLL_glrIm_RunEntropy, wavelet-LLL_glrIm_RunPercentage, wavelet-LLL_glrIm_RunVariance, wavelet-LLL_glrIm_ShortRunLowGrayLevelEmphasis, log-sigma-1-0-mm-3D_glrIm_GrayLevelNonUniformity, log-sigma-1-0-mm-3D_glrIm_LongRunLowGrayLevelEmphasis, log-sigma-1-0-mm-3D_glrIm_RunEntropy, log-sigma-1-0-mm-3D_glrIm_RunPercentage, log-sigma-1-0-mm-3D_glrIm_ShortRunLowGrayLevelEmphasis, log-sigma-2-0-mm-3D_glrIm_GrayLevelNonUniformity, log-sigma-2-0-mm-3D_glrIm_LongRunLowGrayLevelEmphasis, log-sigma-2-0-mm-3D_glrIm_RunEntropy, log-sigma-2-0-mm-3D_glrIm_RunPercentage, log-sigma-2-0-mm-3D_glrIm_ShortRunLowGrayLevelEmphasis, log-sigma-3-0-mm-3D_glrIm_GrayLevelNonUniformity, log-sigma-3-0-mm-3D_glrIm_LongRunLowGrayLevelEmphasis, log-sigma-3-0-mm-3D_glrIm_RunEntropy, log-sigma-3-0-mm-3D_glrIm_RunPercentage, log-sigma-3-0-mm-3D_glrIm_ShortRunLowGrayLevelEmphasis, log-sigma-4-0-mm-3D_glrIm_GrayLevelNonUniformity, log-sigma-4-0-mm-3D_glrIm_LongRunLowGrayLevelEmphasis, log-sigma-4-0-mm-3D_glrIm_RunEntropy, log-sigma-4-0-mm-3D_glrIm_ShortRunLowGrayLevelEmphasis, log-sigma-5-0-mm-3D_glrIm_GrayLevelNonUniformity, log-sigma-5-0-mm-3D_glrIm_LongRunLowGrayLevelEmphasis, log-sigma-5-0-mm-3D_glrIm_RunEntropy, log-sigma-5-0-mm-3D_glrIm_ShortRunLowGrayLevelEmphasis, square_glrIm_GrayLevelNonUniformity, square_glrIm_LongRunLowGrayLevelEmphasis, square_glrIm_RunEntropy, square_glrIm_RunPercentage, square_glrIm_RunVariance, square_glrIm_ShortRunLowGrayLevelEmphasis, squareroot_glrIm_GrayLevelNonUniformity, squareroot_glrIm_LongRunLowGrayLevelEmphasis, squareroot_glrIm_RunEntropy, squareroot_glrIm_RunPercentage, squareroot_glrIm_ShortRunLowGrayLevelEmphasis, logarithm_glrIm_GrayLevelNonUniformity, logarithm_glrIm_LongRunLowGrayLevelEmphasis, logarithm_glrIm_RunEntropy, logarithm_glrIm_RunPercentage, logarithm_glrIm_ShortRunLowGrayLevelEmphasis, exponential_glrIm_GrayLevelNonUniformity, exponential_glrIm_LongRunLowGrayLevelEmphasis, exponential_glrIm_RunEntropy, exponential_glrIm_RunPercentage, exponential_glrIm_RunVariance, exponential_glrIm_ShortRunLowGrayLevelEmphasis, gradient_glrIm_GrayLevelNonUniformity, gradient_glrIm_LongRunLowGrayLevelEmphasis, gradient_glrIm_RunEntropy, gradient_glrIm_RunPercentage, gradient_glrIm_ShortRunLowGrayLevelEmphasis, lbp-3D-m1_glrIm_GrayLevelNonUniformity, lbp-3D-m1_glrIm_LongRunLowGrayLevelEmphasis, lbp-3D-m1_glrIm_RunEntropy, lbp-3D-m1_glrIm_RunPercentage, lbp-3D-m1_glrIm_RunVariance, lbp-3D-m1_glrIm_ShortRunLowGrayLevelEmphasis, lbp-3D-m2_glrIm_GrayLevelNonUniformity, lbp-3D-m2_glrIm_LongRunLowGrayLevelEmphasis, lbp-3D-m2_glrIm_RunEntropy, lbp-3D-m2_glrIm_RunPercentage, lbp-3D-m2_glrIm_RunVariance, lbp-3D-m2_glrIm_ShortRunLowGrayLevelEmphasis, lbp-3D-k_glrIm_GrayLevelNonUniformity, lbp-3D-k_glrIm_LongRunLowGrayLevelEmphasis, lbp-3D-k_glrIm_RunEntropy, lbp-3D-k_glrIm_RunPercentage, lbp-3D-k_glrIm_RunVariance, lbp-3D-k_glrIm_ShortRunLowGrayLevelEmphasis

GLSZM

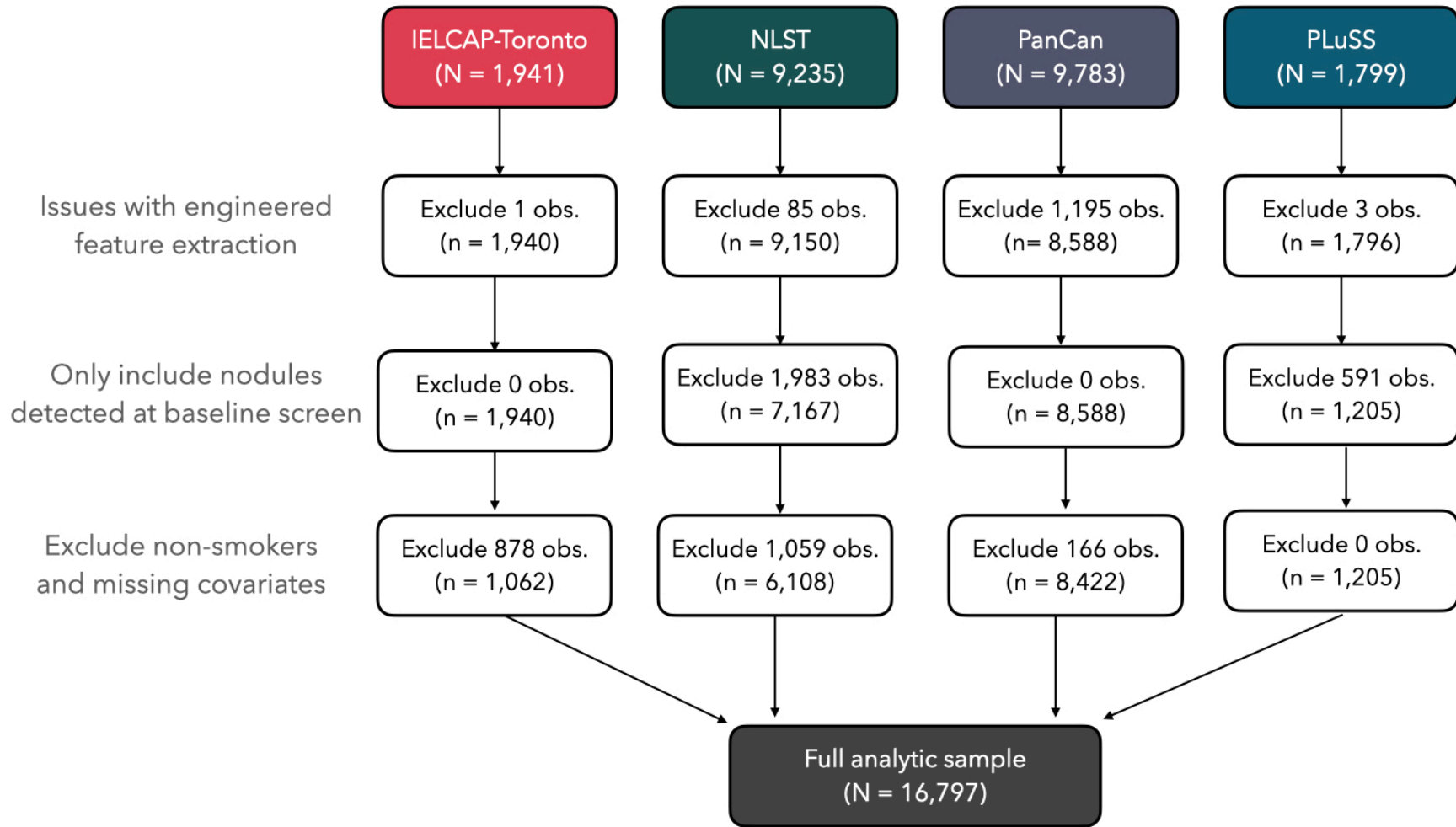
original_glszm_GrayLevelNonUniformity, original_glszm_HighGrayLevelZoneEmphasis, original_glszm_ZonePercentage, wavelet-LLH_glszm_GrayLevelNonUniformity, wavelet-LLH_glszm_ZonePercentage, wavelet-LHL_glszm_GrayLevelNonUniformity, wavelet-LHL_glszm_HighGrayLevelZoneEmphasis, wavelet-LHL_glszm_ZonePercentage, wavelet-LHH_glszm_GrayLevelNonUniformity, wavelet-LHH_glszm_HighGrayLevelZoneEmphasis, wavelet-LHH_glszm_ZonePercentage, wavelet-HLL_glszm_GrayLevelNonUniformity, wavelet-HLL_glszm_HighGrayLevelZoneEmphasis, wavelet-HLL_glszm_ZonePercentage, wavelet-HLH_glszm_GrayLevelNonUniformity, wavelet-HLH_glszm_HighGrayLevelZoneEmphasis, wavelet-HLH_glszm_ZonePercentage, wavelet-HHL_glszm_GrayLevelNonUniformity, wavelet-HHL_glszm_HighGrayLevelZoneEmphasis, wavelet-HHL_glszm_ZonePercentage, wavelet-HHH_glszm_GrayLevelNonUniformity, wavelet-HHH_glszm_HighGrayLevelZoneEmphasis, wavelet-HHH_glszm_ZonePercentage, wavelet-LLL_glszm_GrayLevelNonUniformity, wavelet-LLL_glszm_HighGrayLevelZoneEmphasis, wavelet-LLL_glszm_ZonePercentage, log-sigma-1-0-mm-3D_glszm_GrayLevelNonUniformity, log-sigma-1-0-mm-3D_glszm_HighGrayLevelZoneEmphasis, log-sigma-1-0-mm-3D_glszm_ZonePercentage, log-sigma-2-0-mm-3D_glszm_GrayLevelNonUniformity, log-sigma-2-0-mm-3D_glszm_HighGrayLevelZoneEmphasis, log-sigma-2-0-mm-3D_glszm_ZonePercentage, log-sigma-3-0-mm-3D_glszm_GrayLevelNonUniformity, log-sigma-3-0-mm-3D_glszm_HighGrayLevelZoneEmphasis, log-sigma-3-0-mm-3D_glszm_ZonePercentage, log-sigma-4-0-mm-3D_glszm_GrayLevelNonUniformity, log-sigma-4-0-mm-3D_glszm_HighGrayLevelZoneEmphasis, log-sigma-4-0-mm-3D_glszm_ZonePercentage, log-sigma-5-0-mm-

	<p>3D_glszm_GrayLevelNonUniformity, log-sigma-5-0-mm-3D_glszm_HighGrayLevelZoneEmphasis, log-sigma-5-0-mm-3D_glszm_ZonePercentage, square_glszm_GrayLevelNonUniformity, square_glszm_ZonePercentage, squareroot_glszm_GrayLevelNonUniformity, squareroot_glszm_HighGrayLevelZoneEmphasis, squareroot_glszm_ZonePercentage, logarithm_glszm_GrayLevelNonUniformity, logarithm_glszm_HighGrayLevelZoneEmphasis, logarithm_glszm_ZonePercentage, exponential_glszm_GrayLevelNonUniformity, exponential_glszm_ZonePercentage, gradient_glszm_GrayLevelNonUniformity, gradient_glszm_ZonePercentage, lbp-3D-m1_glszm_ZonePercentage, lbp-3D-m2_glszm_ZonePercentage, lbp-3D-k_glszm_GrayLevelNonUniformity, lbp-3D-k_glszm_HighGrayLevelZoneEmphasis, lbp-3D-k_glszm_ZonePercentage</p>
NGTDM	<p>original_ngtdm_Busyness, original_ngtdm_Complexity, original_ngtdm_Contrast, original_ngtdm_Strength, wavelet-LLH_ngtdm_Busyness, wavelet-LLH_ngtdm_Contrast, wavelet-LLH_ngtdm_Strength, wavelet-LHL_ngtdm_Busyness, wavelet-LHL_ngtdm_Complexity, wavelet-LHL_ngtdm_Contrast, wavelet-LHL_ngtdm_Strength, wavelet-LHH_ngtdm_Busyness, wavelet-LHH_ngtdm_Complexity, wavelet-LHH_ngtdm_Contrast, wavelet-LHH_ngtdm_Strength, wavelet-HLL_ngtdm_Busyness, wavelet-HLL_ngtdm_Complexity, wavelet-HLL_ngtdm_Contrast, wavelet-HLL_ngtdm_Strength, wavelet-HLH_ngtdm_Busyness, wavelet-HLH_ngtdm_Complexity, wavelet-HLH_ngtdm_Contrast, wavelet-HLH_ngtdm_Strength, wavelet-HHL_ngtdm_Busyness, wavelet-HHL_ngtdm_Complexity, wavelet-HHL_ngtdm_Contrast, wavelet-HHL_ngtdm_Strength, wavelet-HHH_ngtdm_Busyness, wavelet-HHH_ngtdm_Complexity, wavelet-HHH_ngtdm_Contrast, wavelet-HHH_ngtdm_Strength, wavelet-LLL_ngtdm_Complexity, wavelet-LLL_ngtdm_Contrast, wavelet-LLL_ngtdm_Strength, log-sigma-1-0-mm-3D_ngtdm_Busyness, log-sigma-1-0-mm-3D_ngtdm_Contrast, log-sigma-1-0-mm-3D_ngtdm_Strength, log-sigma-2-0-mm-3D_ngtdm_Busyness, log-sigma-2-0-mm-3D_ngtdm_Complexity, log-sigma-2-0-mm-3D_ngtdm_Contrast, log-sigma-2-0-mm-3D_ngtdm_Strength, log-sigma-3-0-mm-3D_ngtdm_Complexity, log-sigma-3-0-mm-3D_ngtdm_Contrast, log-sigma-3-0-mm-3D_ngtdm_Strength, log-sigma-4-0-mm-3D_ngtdm_Complexity, log-sigma-4-0-mm-3D_ngtdm_Contrast, log-sigma-4-0-mm-3D_ngtdm_Strength, log-sigma-5-0-mm-3D_ngtdm_Complexity, log-sigma-5-0-mm-3D_ngtdm_Contrast, log-sigma-5-0-mm-3D_ngtdm_Strength, square_ngtdm_Busyness, square_ngtdm_Contrast, square_ngtdm_Strength, squareroot_ngtdm_Busyness, squareroot_ngtdm_Complexity, squareroot_ngtdm_Contrast, squareroot_ngtdm_Strength, logarithm_ngtdm_Complexity, logarithm_ngtdm_Contrast, logarithm_ngtdm_Strength, exponential_ngtdm_Strength, gradient_ngtdm_Busyness, gradient_ngtdm_Complexity, gradient_ngtdm_Contrast, gradient_ngtdm_Strength, lbp-3D-k_ngtdm_Busyness, lbp-3D-k_ngtdm_Complexity, lbp-3D-k_ngtdm_Strength, wavelet-LLH_ngtdm_Coarseness, wavelet-LHL_ngtdm_Coarseness, wavelet-LHH_ngtdm_Coarseness, wavelet-HLL_ngtdm_Coarseness, wavelet-HLH_ngtdm_Coarseness, wavelet-HHL_ngtdm_Coarseness, wavelet-HHH_ngtdm_Coarseness, wavelet-LLL_ngtdm_Coarseness, original_ngtdm_Coarseness</p>
21	
Shape (3D)	<p>original_shape_Elongation, original_shape_Flatness, original_shape_LeastAxisLength, original_shape_Sphericity</p>

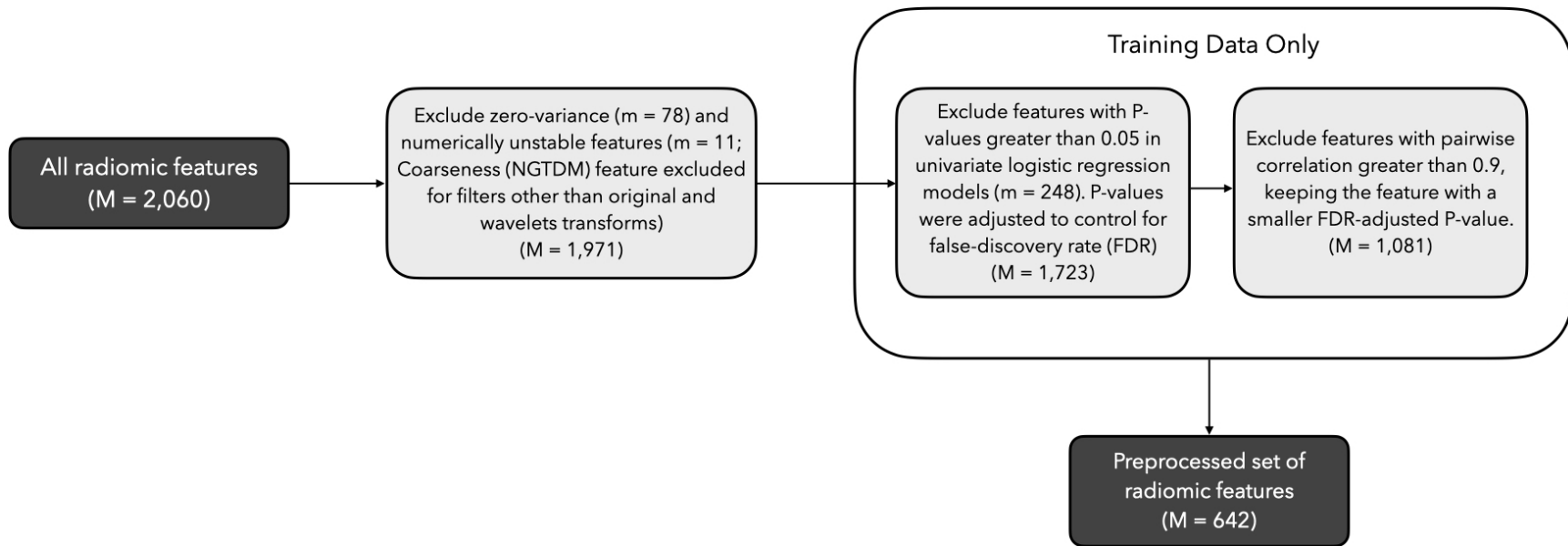
Supplemental Table 7. Area under the receiver operating characteristic curves and bootstrap-based 95% confidence intervals for the INTEGRAL-Radiomics and PanCan model in the held-out test data based on key patient-related and nodule-related factors.

	INTEGRAL-Radiomics (N = 13,434)	PanCan (N = 3,363)
Overall	0.930 (0.901-0.957)	0.868 (0.847, 0.888)
Nodule solidity		
Solid	0.928 (0.891-0.964)	0.880 (0.855-0.903)
Subsolid	0.909 (0.853-0.954)	0.828 (0.789-0.863)
Nodule major axis length		
< 10 mm	0.811 (0.677-0.927)	0.722 (0.668-0.776)
≥ 10 mm	0.889 (0.842-0.926)	0.779 (0.751-0.807)
5-15 mm	0.799 (0.709-0.880)	0.817 (0.786-0.846)
5-30 mm	0.889 (0.840-0.932)	0.851 (0.830-0.872)
Sex		
Male	0.918 (0.870-0.958)	0.857 (0.830-0.884)
Female	0.943 (0.905-0.971)	0.885 (0.859-0.909)
Age at baseline		
< 65 years	0.944 (0.903-0.977)	0.881 (0.854-0.906)
≥ 65 years	0.910 (0.861-0.952)	0.842 (0.812-0.875)
Smoking status		
Current	0.945 (0.910-0.973)	0.852 (0.820-0.879)
Former	0.914 (0.859-0.955)	0.885 (0.860-0.909)

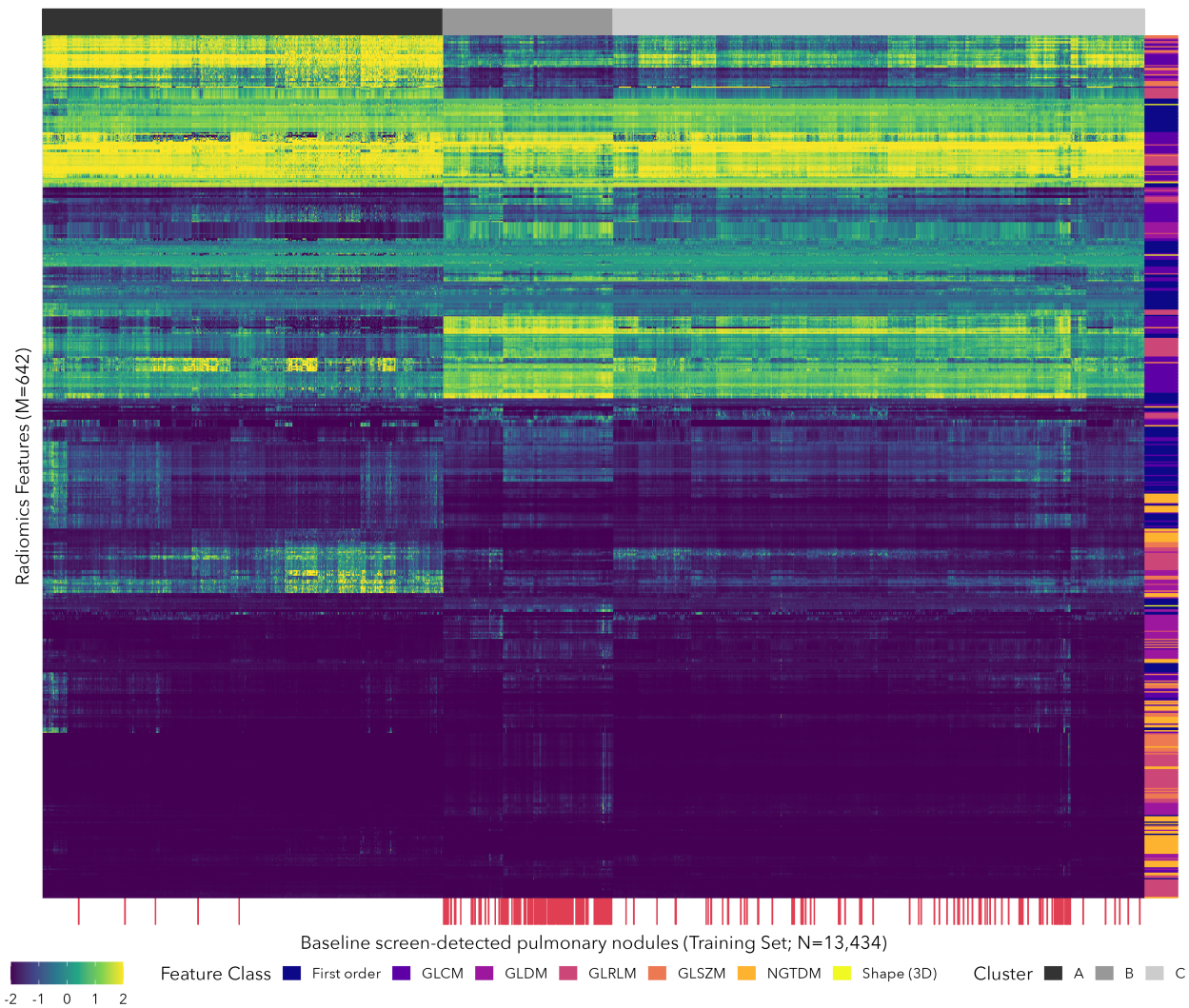
Abbreviations: AUC, area under the curve; CI, confidence interval; mm, millimetre.



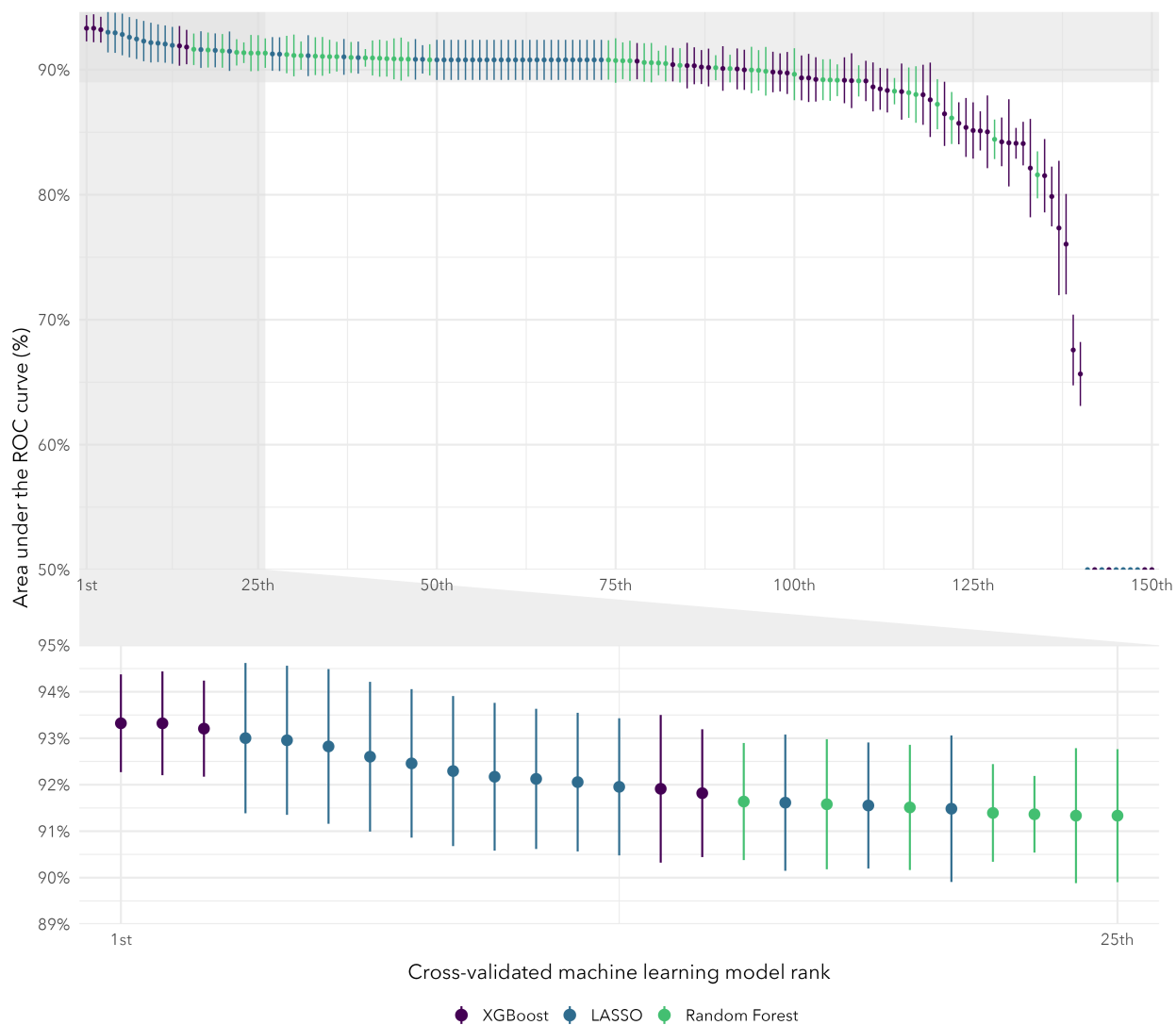
Supplemental Figure 1. Flow chart for the number of nodules retained for each of the four lung cancer screening studies based on sequential data cleaning steps to remove: (1) any nodules with feature extraction issues, (2) any nodules detected beyond the baseline CT scans, and (3) observations with missing patient-level epidemiologic data.



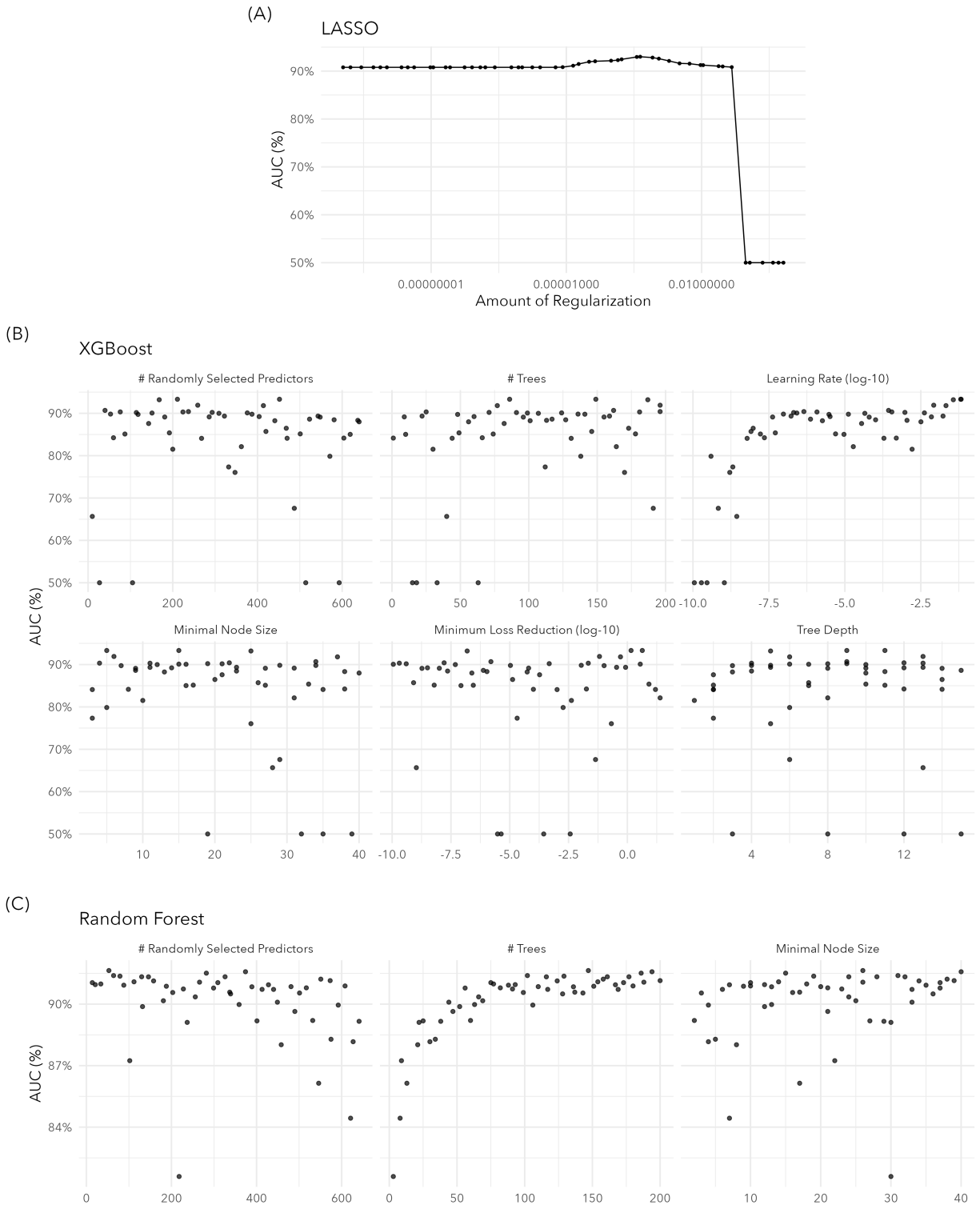
Supplemental Figure 2. Flow chart for the radiomics feature pre-processing steps to filter out (1) zero-variance and numerically unstable features, (2) non-significant features based on univariate p-values in the training data, and (3) highly correlated features in the training data, keeping the more significant feature.



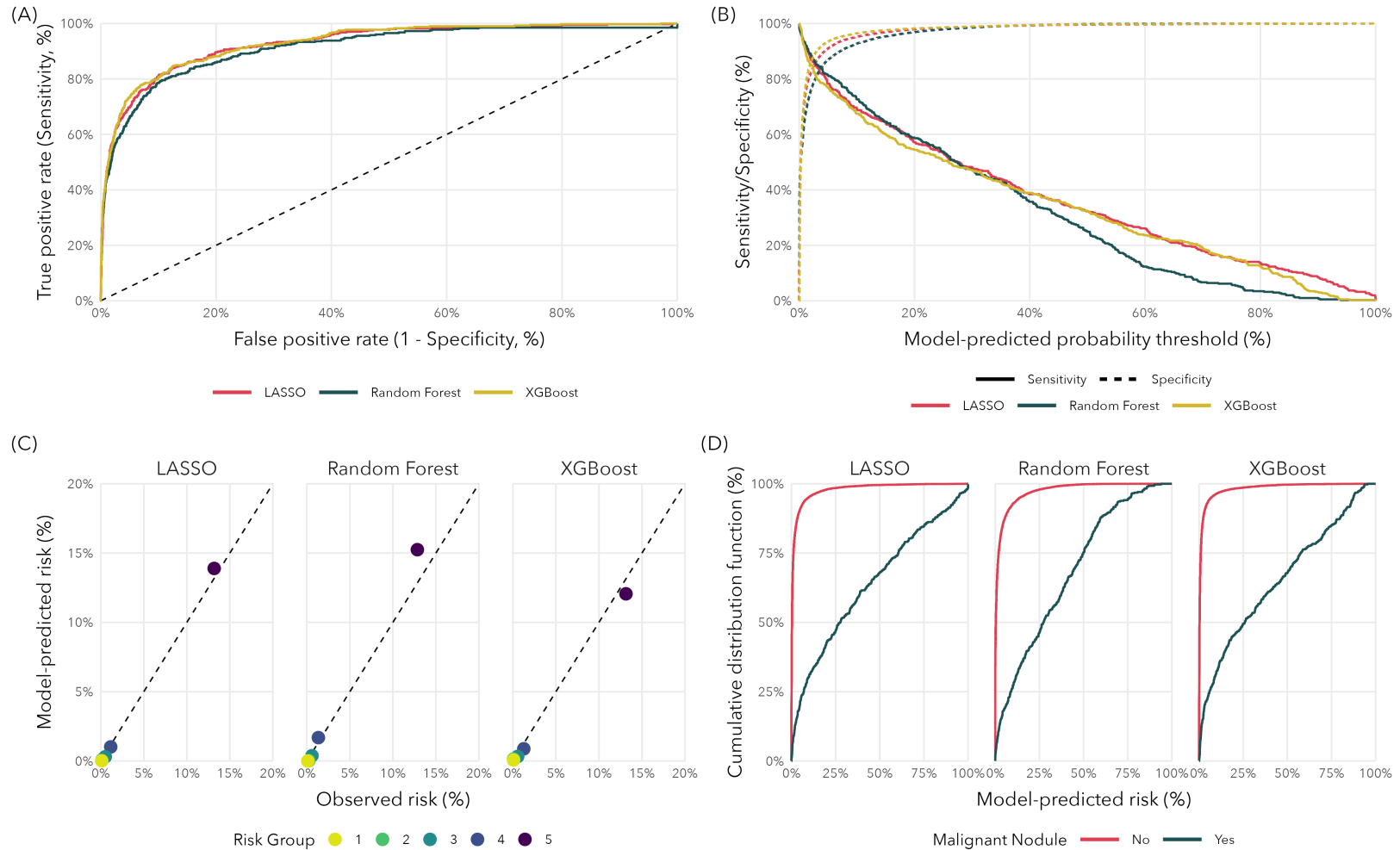
Supplemental Figure 3. Heat map for the 642 radiomics features retained in the feature filtering steps based on the training data (See Supplemental Figure 2). Features were min-max rescaled to the range [-2,2]. Three distinct clusters (i.e., radiomic profiles) were identified (indicated by the gray boxes along the top axis) and they differed significantly with respect to the proportion of malignant nodules (Fishers exact P-value < 0.05). Class membership for the 642 radiomic features are indicated along the right axis. Malignant nodules are indicated along the bottom axis.



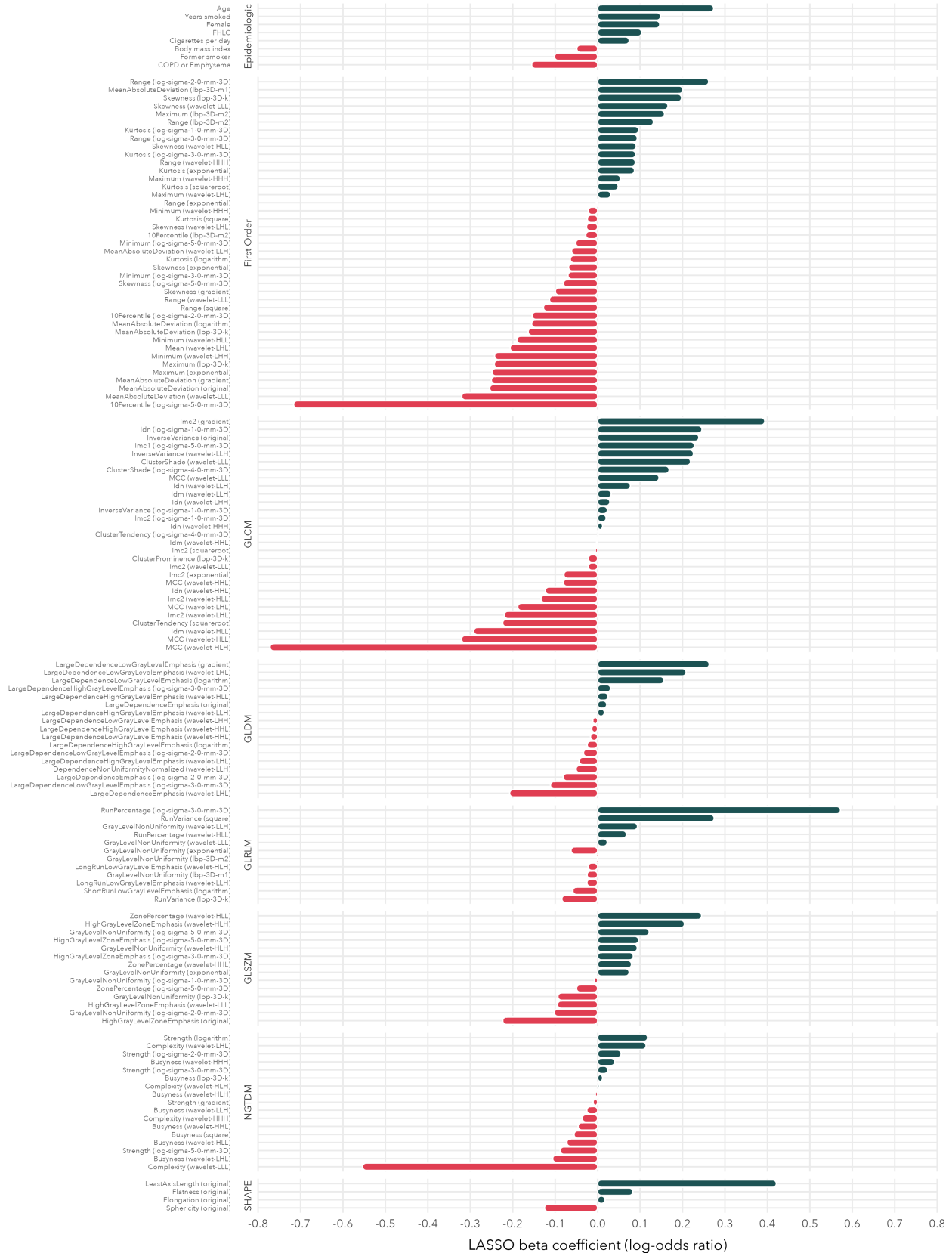
Supplemental Figure 4. Cross-validated area under the receiver operating characteristic curve (AUC) and 95% confidence intervals for each of the hyperparameter combinations (i.e., submodels) for the machine learning models. Models are ordered from left-to-right based on descending AUC. The top panel shows the rankings for every submodel and the bottom panel zooms in on the top 25 submodels.



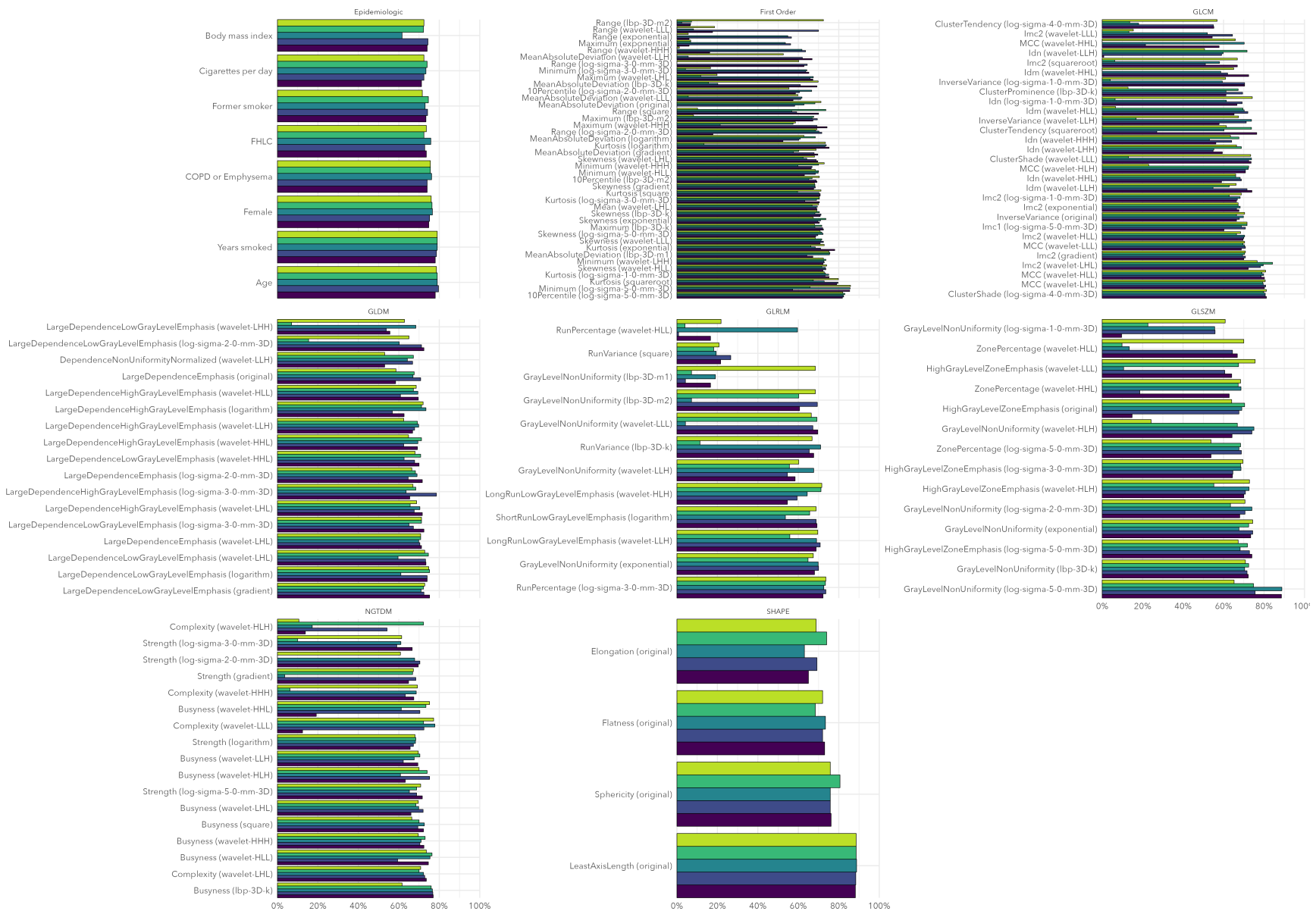
Supplemental Figure 5. Results from the five-fold cross-validation used to determine the top performing machine learning model. Area under the curve (AUC) are presented according to hyperparameters for (A) LASSO, (B) XGBoost, and (C) Random Forest.



Supplemental Figure 6. Model performance metrics for the three top-performing machine learning models selected based on cross-validated area under the receiver operating characteristic curve (LASSO, Random Forest, XGBoost). (A) Receiver operating characteristic curves. (B) Sensitivity and specificity across the range of model-predicted probabilities. (C) Calibration plots comparing observed and model-predicted risks within quintiles of model-predicted risks. (D) Cumulative distribution functions of the model-predicted risks for benign and malignant pulmonary nodules.



Supplemental Figure 7. Beta coefficients for the predictors retained in the final LASSO model with non-zero coefficients. Predictors are grouped by feature class. The image transformation associated with a radiomic feature is listed in parentheses.



Supplemental Figure 8. Feature stability for the radiomic and epidemiologic features included in our INTEGRAL-Radiomics model based on cross-validation. The percentage (x-axis) represents the number of times a feature was retained in the LASSO model (non-zero coefficient) for each fold and across all penalty (lambda) values.